Scripta Materialia 142 (2018) 133–137

Contents lists available at ScienceDirect

Scripta Materialia

journal homepage: www.elsevier.com/locate/scriptamat

Regular article

Magnetic properties and crystallization kinetics of $(Fe_{100-x}Ni_x)_{80}Nb_4Si_2B_{14}$ metal amorphous nanocomposites

Natan Aronhime [a,*], Eli Zoghlin [a], Vladimir Keylin [a,b,c], Xin Jin [a], Paul Ohodnicki [d], Michael E. McHenry [a]

[a] Carnegie Mellon University, Pittsburgh, PA 15221, United States
[b] NASA Glenn Research Center, Cleveland, OH 44135, United States
[c] Vantage Partners LLC, Brook Park, OH 44142, United States
[d] National Energy Technology Laboratory, Pittsburgh, PA 15236, United States

ARTICLE INFO

Article history:
Received 7 August 2017
Received in revised form 23 August 2017
Accepted 27 August 2017

Keywords:
Soft magnetic materials
Nanocomposites
Crystallization kinetics

ABSTRACT

Fe-Ni based metal amorphous nanocomposites (MANCs) are investigated in the pseudo-binary alloys $(Fe_{100-x}Ni_x)_{80}Nb_4Si_2B_{14}$. To optimize the soft magnetic properties of the nanocomposites, primary and secondary crystallization kinetics must be understood. As such, primary and secondary crystallization temperatures are determined by differential scanning calorimetry, and activation energies are calculated, along with the resulting crystalline phases. Time-temperature-transformation diagrams for primary and secondary crystallization in $(Fe_{70}Ni_{30})_{80}Nb_4Si_2B_{14}$ are presented. Saturation magnetization and Curie temperature are determined. Lastly, the shape of magnetization vs. time curves for $(Fe_{30}Ni_{70})_{80}Nb_4Si_2B_{14}$ at various temperatures suggest that the secondary crystal product often consumes some of the primary crystalline product.

Metal amorphous nanocomposite (MANC) soft magnetic materials (SMMs) are materials produced through controlled primary nanocrystallization of amorphous precursors. They are of current interest for power converter [1,2] and motor applications [3,4]. If used at higher frequencies, motors and converters can be reduced in size to maintain the same power output. Conventional materials, like silicon steels, are lossy at high frequency because of their smaller electrical resistivities and inability to cast and roll to 10′s of μm thickness [3,4]. These limitations are evident from eddy current losses as expressed by:

$$P_e = \frac{(\pi \times t)^2}{\rho} f^2 B^2 \quad (1)$$

where t is thickness, ρ is resistivity, f is frequency, and B is induction. MANC materials can exhibit higher efficiencies due to high resistivities and low and tunable anisotropies [1,3,5–7].

Fe-Co and Co-based MANCs have recently been investigated as promising candidates for transformer applications [6,8–12]. Fe-Ni nanocomposite alloys are of interest due to the lower cost of Ni compared to Co while maintaining many of the benefits over Fe-based nanocomposites that Co-based alloys enjoy [3,8,13]. Fe-, FeCo-, and Co-based MANCs are analogous to similar materials classes in amorphous magnets. FeNi-based MANCs are a more recent class, also analogous to amorphous magnets, previously investigated at compositions with near room temperature Curie temperatures for magnetocaloric applications [14]. A wider compositional range in Fe-Ni- based MANCs is reported here that includes saturation inductions and Curie temperatures suitable for power applications. In certain composition ranges, they also exhibit longitudinal stress induced anisotropy useful for high permeability engineering required for motor applications [15].

MANCs are produced by planar flow casting an amorphous ribbon. The resulting ribbon is then heat treated to induce primary crystallization (at temperatures typically ~500 °C but depending on composition). Primary crystallization concentrates the magnetic elements in nanocrystals, and for appropriate compositions leaves the amorphous matrix ferromagnetic allowing two magnetic phase microstructures where random magnetic anisotropy described by Herzer [5] leads to low DC hysteretic losses. The resistive amorphous phase and chemical partitioning [7] are beneficial to the AC magnetic properties of the material in reducing classical eddy current losses. At higher temperatures (typically 600–650 °C) secondary crystallization consumes the remaining amorphous phase resulting in a magnetically hard phase, which is deleterious to the soft magnetic properties [16].

Due to the deleterious properties of secondary crystallization, the kinetics of primary and secondary crystallization in MANCs must be understood. The kinetics is strongly dependent on chemical composition and has been studied previously for FINEMET, NANOPERM, HITPERM, and Co-rich alloys [17–20]. In this regard, the development of MANCs mirrors that of amorphous magnetic alloys [21], but little analysis of crystallization kinetics has been done on the Fe-Ni MANC system.

* Corresponding author.
E-mail address: naronhim@andrew.cmu.edu (N. Aronhime).

http://dx.doi.org/10.1016/j.scriptamat.2017.08.043
1359-6462/

Crystallization is a solid-state transformation typically controlled by nucleation and growth. The extent of a phase transformation can be represented by plotting the volume fraction transformed as a function of temperature and time in a TTT diagram. The kinetics required to construct a TTT diagram can be derived from Johnson-Mehl-Avrami-Kolmogorov (JMAK) kinetics. With JMAK kinetics, the rate constant, k, is expressed as:

$$k = k_0 \exp\left(\frac{-Q}{k_B T}\right) \quad (2)$$

where Q is the activation energy for crystallization, T is temperature, k_B is the Boltzmann constant, and k_0 is the rate constant coefficient. The JMAK equation for volume fraction transformed can then be written:

$$X = 1 - \exp(-(k(t-t_i))^n) \quad (3)$$

where t_i is the incubation time, and n is between 1 and 4 depending on dimensionality and the nucleation and growth mechanism.

JMAK kinetics does not fully take in account the mechanisms for crystallization in MANCs however. This is because during crystallization, the early transition metals are expelled from the crystallites and form a diffusion barrier limiting further crystallite growth. These diffusion barriers produce impinging diffusion fields instead of direct impingement of the crystallites [22,23]. In this work, we begin to examine the crystallization kinetics for Fe-Ni based MANCs. In the pseudo-binary $(Fe_{100-x}Ni_x)_{80}Nb_4Si_2B_{14}$ ($10 \le x \le 80$) alloys reported here Si and B are metalloid glass formers and Nb the early transition metal growth inhibitor. Nb, as compared with other early transition metals (e.g. Hf [24], Zr [25]) is beneficial for rapid solidification processing in air which is also more commercially viable.

Ingots with composition of $(Fe_{100-x}Ni_x)_{80}Nb_4Si_2B_{14}$ ($10 \le x \le 80$) were produced by melting stoichiometric amounts of the constituent elements (minimum purity of 99.8%) in a Lincoln IDEALARC arc-melter until homogenized. The ingots were cast into a ribbon using planar flow casting with an Edmund-Buhler Melt Spinner SC outfitted with a Cu-alloy wheel under an Ar atmosphere. Ribbons were determined to be amorphous by first employing a bend test of ductility [26] and then by XRD using a PANalytical X'Pert PRO. XRD scans were over 2θ values of 30°–80° with a scan rate of 0.9°/min. Al_2O_3 powder is put on top of the surface to help align the z-position of the sample. DSC was carried out on a Perkin-Elmer DSC 8500 unit with Cu pans and heating rates of 20 °C/min, 40 °C/min, and 60 °C/min. Magnetometry was performed on a Lakeshore 7400-S vibrating sample magnetometer (VSM) with a 1000 °C inert gas (Ar) furnace and a heating rate of 2 °C/min was used for temperature dependent measurements. A fixed field of 5000 Oe was used for all magnetic measurements. DSC was done using a Perkin Elmer 8500 device. TTT diagrams were determined using a method similar to that used by DeGeorge et al. [16].

Primary and secondary crystallization temperatures are shown in Fig. 1(a) as a function of the average number of s and d electrons per metal atom in the alloy. Primary crystallization is defined as the event during which the transition metals, in this case Fe and Ni, crystallize. Secondary crystallization is defined as when the remaining glass former enriched amorphous phase crystallizes. Electrons per atom is determined by calculating the number of electrons per transition metal atom as a function of alloy composition [27]. Fig. 1(b) shows a typical DSC curve with clear primary and secondary exothermic crystallization events. The glass formers are identical in all compositions, with only the relative amounts of Fe and Ni changing. Because Fe and Ni have nearly identical atomic diameters, the systematic variation in the crystallization temperatures is strongly correlated with electron concentration [17] and the bonding characteristics of the alloy. It has been previously proposed that the bonds produced by the overlap between the s-p orbitals of the metalloids and the s-d orbitals of the transition metals are strengthened by a lower number of d-electrons, or a lower e/a value,

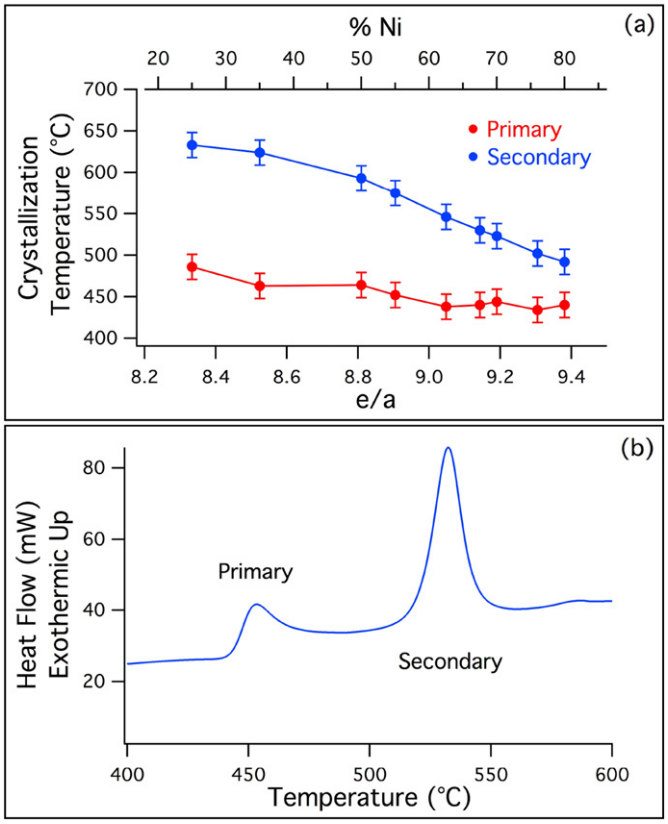

Fig. 1. (a) Crystallization temperature vs. electrons/atom. (b) Typical DSC curve showing exothermic peaks for primary and secondary crystallization with a heating rate of 40 °C/min.

thereby stabilizing the amorphous phase. A lower e/a value corresponds to increasing the number of bonding states, while a higher e/a value increases the number of antibonding states [27].

This stabilization at higher Fe contents can also be viewed from the perspective of the Friedel model [28] of the density of states. With the Friedel model, a roughly parabolic cohesive energy, E_C, can be calculated as a function of element across a period [28–30]. The E_C for crystalline Fe is weaker than for Ni [30], so it could be expected for the amorphous phase to be more stable with respect to secondary crystallization as the alloy is enriched in Fe. This is because with higher Fe content, the energy is lowered by a smaller amount with crystallization as compared to a Ni-rich alloy. This correlates with previous reports that Ni-based amorphous alloys easily undergo secondary crystallization because the other transition metal elements stabilize the 23:6 phase more than in Fe-based alloys [31].

The activation energies for primary (Q_1) and secondary (Q_2) crystallization, and the difference between the two are depicted in Fig. 2(a). Activation energies were determined by the Kissinger method [32,33]. The Kissinger equation is:

$$\ln\left(\frac{\alpha}{T_x^2}\right) = -\frac{Q}{RT_x} + c \quad (4)$$

where α is the heating rate and T_x is the crystallization temperature, Q is the activation energy, R is the gas constant, and c is an integration constant. Similar to crystallization temperatures, the values of Q for primary and secondary crystallization approach one another at high Ni contents. This implies that the remaining amorphous phase after primary crystallization in Ni-rich alloys is less stable than the remaining amorphous phase in Fe-rich alloys. It is also possible that the kinetic barrier to diffusion is lower with higher Ni content, and that allows the amorphous

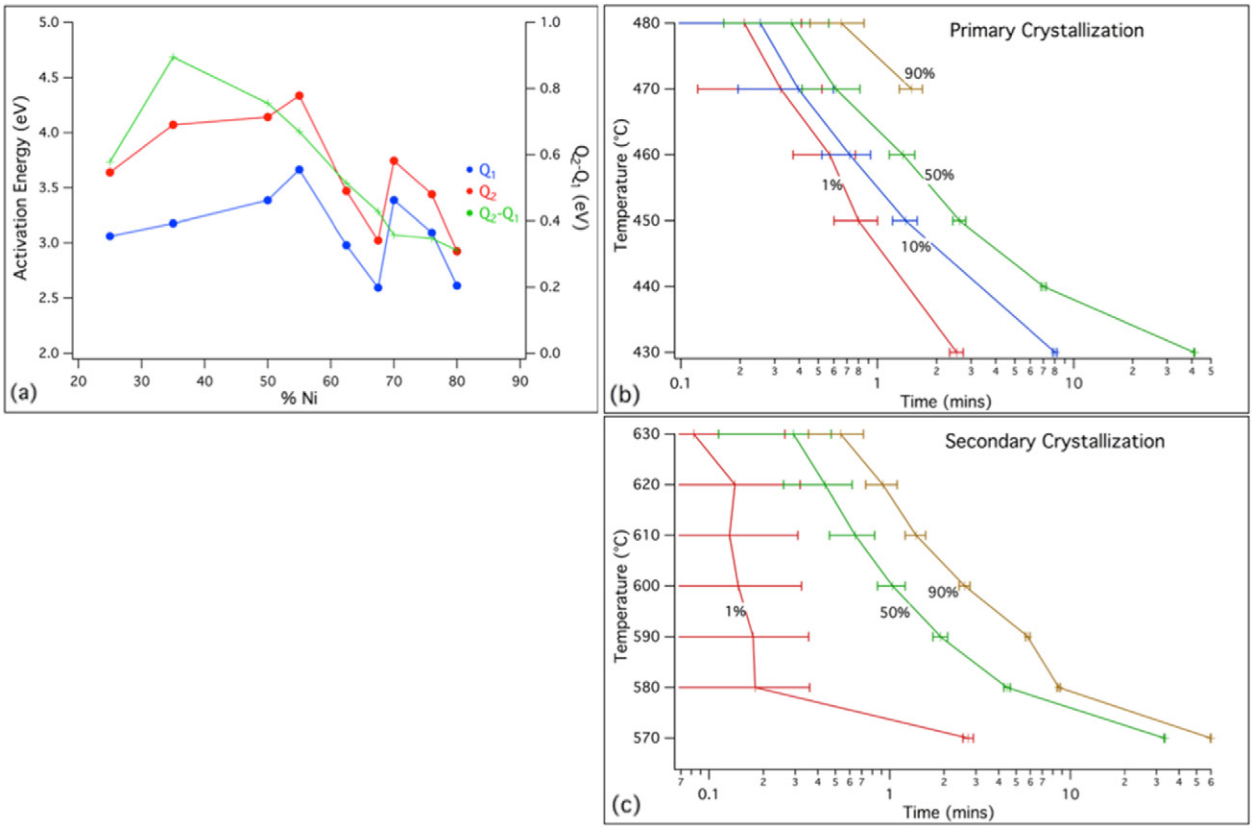

Fig. 2. (a) Activation energy for primary and secondary crystallization as a function of % Ni. TTT diagram for (b) primary and (c) secondary crystallization for $(Fe_{70}Ni_{30})_{80}Nb_4Si_2B_{14}$.

phase to crystallize more easily. While polymorphic transformations are observed in Co-based alloys, they have not been observed in Ni-based MANCs [6,12].

Developing the proper microstructure in MANCs is critical to optimizing the magnetic properties. To this end, it is beneficial to have a time-temperature-transformation (TTT) diagram for primary crystallization. In addition, due to the deleterious effects of secondary crystallization, it is important to know that a MANC device will not undergo secondary crystallization during the projected lifetime of a device at operating temperature. Because $(Fe_{70}Ni_{30})_{80}Nb_4Si_2B_{14}$ is of particular interest [15], TTT diagrams were determined for this alloy and can be seen in Fig. 2(b) and (c) . Using this data and Eqs. (2) and (3), stability at lower temperatures and longer times can be predicted.

First, the Avrami exponent can be determined using the Augis and Bennett [34] method:

$$n = \frac{2.5}{\Delta\tau_{FWHM}} \frac{T_m^2}{Q} \tag{5}$$

where $\Delta\tau_{FWHM}$ is the full width at half maximum of the DSC peak, and T_m is the temperature at the DSC peak. For $(Fe_{70}Ni_{30})_{80}Nb_4Si_2B_{14}$, this yields an n value of 2.5, which is consistent with constant nucleation and 3-dimensional diffusion controlled growth. Using the data from the TTT diagram, k values can be calculated with Eq. (3), and k_0 values with Eq. (2). Each data point will yield somewhat different k_0 values, so this variance can be used to estimate the error in the calculations. Then, with values for k_0 and k, X can be estimated at lower temperatures and longer times. Since it is of interest to demonstrate the stability of the amorphous phase at possible device operation temperatures, time and temperatures are calculated for 1% secondary crystallization. At 200 °C, 1% secondary crystallization is not predicted to occur for $9 \times 10^{11} \pm 6 \times 10^{11}$ years, and at 300 °C, 50,000 ± 30,000 years are predicted. At 350 °C, only 90 ± 60 years are predicted, and at 400 °C, the amorphous phase is predicted to be stable for less than a year.

Crystallization products are identified by XRD, with a low Ni and a high Ni alloy shown in Fig. 3. In most alloys, the primary crystallites are identified as γ-FeNi. In $(Fe_{75}Ni_{25})_{80}Nb_4Si_2B_{14}$ alloys, the primary crystallites are initially α-FeNi, but γ-FeNi comes out at higher temperatures (Fig. 3b). While the Fe-Ni phase diagram shows a significant α + γ coexistence region, it is possible the effective local compressive stress due to the lower density of the amorphous phase [35] relative to the crystalline phase stabilizes the γ-phase at higher Fe contents then would be expected otherwise. The α- to γ- phase transition in Fe-based nanocomposites [36] is an area of much current interest and suggests future studies of Fe-rich alloys under pressure. The secondary crystallization product is identified as $(FeNi)_{23}B_6$ phase with the $Cr_{23}C_6$ prototype structure [31,37,38].

Magnetization and Curie temperature (T_C) data for as-cast ribbons are shown in Fig. 4(a) along with T_c of γ-FeNi. As expected, the saturation magnetization decreases with increasing Ni content. Comparing T_C of γ-FeNi to the T_C of the amorphous phase shows a shift of the peak T_C from 70% Ni to 30% [39]. This can be understood qualitatively with respect to the Bethe-Slater curve [40,41]. The Bethe-Slater curve plots the magnetic exchange interaction as a function of atomic separation normalized by the diameter of the d-electron orbital, and resembles an inverted potential well diagram. In the amorphous phase, there is a distribution of atomic spacings which contribute to a distribution of exchange energies [42]. Fe-Fe interactions in the γ phase are negative, and extremely sensitive to atomic spacing while Ni-Ni and Fe-Ni interactions are positive and not as sensitive. It is for this reason that the peak in Curie temperature lies on the Ni-rich side of the binary phase diagram for the γ phase. Since Fe atoms bond distances cannot get much smaller than observed in close-packed structures and the amorphous phase typically has ~2% free volume, the distribution will be weighted to larger spacings, which can lead to some positive Fe—Fe exchange

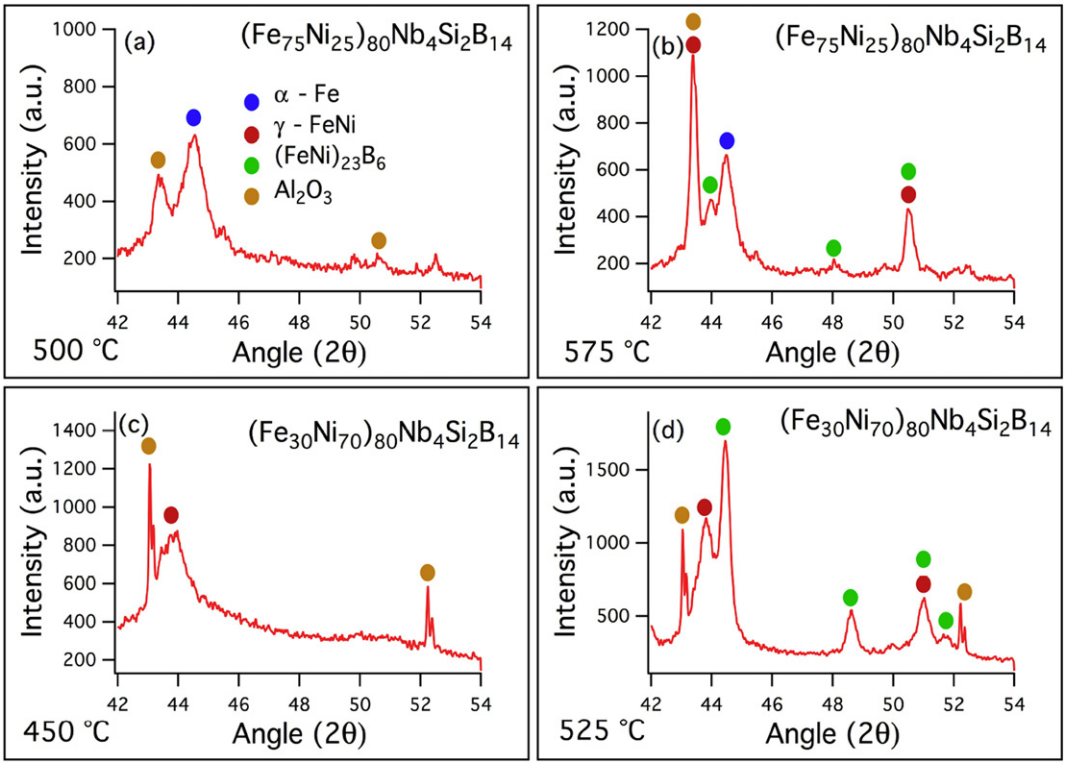

Fig. 3. (a) and (b) $(Fe_{75}Ni_{25})_{80}Nb_4Si_2B_{14}$ at heated to 500 °C and 575 °C respectively. (c) and (d) $(Fe_{30}Ni_{70})_{80}Nb_4Si_2B_{14}$ heated to 450 °C and 525 °C respectively.

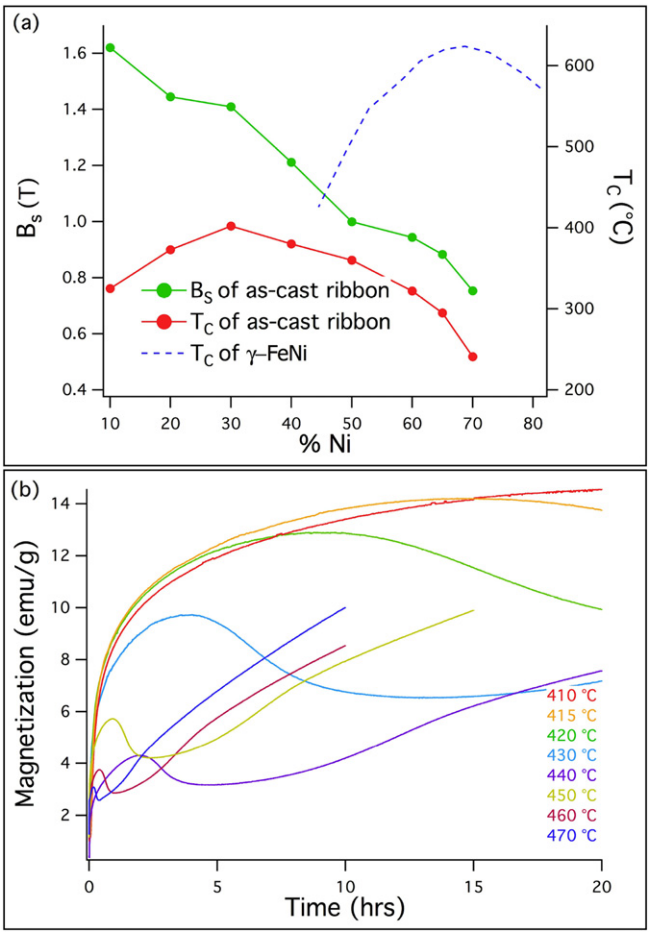

Fig. 4. (a) As-cast saturation induction and T_c, and γ-FeNi T_c. (b) Magnetization vs. time at temperature for $(Fe_{30}Ni_{70})_{80}Nb_4Si_2B_{14}$.

interactions. It is therefore expected that the peak in T_C will shift to higher Fe contents with respect to γ-FeNi. The overall decrease in T_C can be explained by the fact that the alloy has a significant number of non-magnetic atoms that do not contribute to the overall exchange energy. Also, the total exchange energy may be lower due to the averaging of positive and negative exchange interactions among the Fe-Fe interactions.

Fig. 4(b) depicts magnetization as a function of time at various temperatures for a $(Fe_{30}Ni_{70})_{80}Nb_4Si_2B_{14}$ sample. At all temperatures above 420 °C, the magnetization reaches a maximum, decreases, and then increases again. In order for this to occur, the secondary crystallites must consume some of the crystals formed during primary crystallization. Secondary crystallization occurs at these low temperatures due to the relative instability of the amorphous phase in high Ni alloys, and possibly also due to lower migrational energy as noted earlier. With higher Fe, secondary crystallization is not observed at lower temperatures. The decrease in the maximum magnetization is due to approaching the Curie temperature of the primary crystallites (~500 °C).

As primary crystallization occurs, the amorphous matrix becomes enriched in glass forming atoms. Once the ratio of Fe and Ni to B and Nb lowers enough, the amorphous matrix may be able to undergo a diffusionless polymorphic transition to the 23:6 phase [12]. This will be tested in the future with more extensive M vs. T experiments.

Fe-Ni based amorphous nanocomposites were investigated. Crystallization temperatures and energies were found to approach one another with higher Ni contents. The primary crystallites were identified as γ-FeNi for all alloys except $(Fe_{75}Ni_{25})_{80}Nb_4Si_2B_{14}$. For this alloy, primary crystallites were α-FeNi with γ-FeNi forming at higher temperatures. All alloys showed $(FeNi)_{23}B_6$ as the secondary crystallization product. TTT diagrams for primary and secondary crystallization in $(Fe_{70}Ni_{30})_{80}Nb_4Si_2B_{14}$ were shown, and stability calculations were carried out predicting the stability of the amorphous phase over 20 years for several temperatures. Magnetometry demonstrates that saturation inductions of >1.5 T are possible with Fe-Ni MANCs. It also suggests that the secondary crystal product consumes some of the primary crystal product when forming.

N.A. would like to thank P.O. for running the HTXRD at NETL. The authors also acknowledge support from the DOE Solar Energy Technology Office and the Grid Modernization Laboratory Consortium through the SuNLaMP initiative under agreement # DE-EE-00031004. MEM acknowledges support from the DOE AMO program through DOE/EERE – Office of Advanced Manufacturing Program Award Number: DE-EE0007867.

References

[1] A.M. Leary, P.R. Ohodnicki, M.E. McHenry, JOM 64 (2012) 772–781.
[2] F. Mazaleyrat, L.K. Varga, J. Magn. Magn. Mater. 215 (2000) 253–259.
[3] J.M. Silveyra, A.M. Leary, V. DeGeorge, S. Simizu, M.E. McHenry, J. Appl. Phys. 115 (2014), 17A319.
[4] J.M. Silveyra, P. Xu, V. Keylin, V. DeGeorge, A. Leary, M.E. McHenry, J. Electron. Mater. 45 (2016) 219–225.
[5] G. Herzer, in: B. Idzikowski, P. Svec, M. Miglierini (Eds.), NATO Sci. Ser. II Math. Phys. Chem., Kluwer Academic, Budmerice, Slovakia, 2003.
[6] M.E. McHenry, D.E. Laughlin, Phys. Metall, 5th ed., 2015.
[7] A. Leary, V. Keylin, A. Devaraj, V. DeGeorge, P. Ohodnicki, M.E. McHenry, J. Mater. Res. 23 (2016) 1–19.
[8] V. Degeorge, S. Shen, P. Ohodnicki, M. Andio, M.E. McHenry, J. Electron. Mater. 43 (2014) 96–108.
[9] A.M. Leary, V. Keylin, P.R. Ohodnicki, M.E. McHenry, J. Appl. Phys. 117 (2015), 17A338.
[10] S. Shen, P.R. Ohodnicki, S.J. Kernion, M.E. McHenry, J. Appl. Phys. 112 (2012) 103705.
[11] P.R. Ohodnicki, Y.L. Qin, D.E. Laughlin, M.E. McHenry, M. Kodzuka, T. Ohkubo, K. Hono, M.A. Willard, Acta Mater. 57 (2009) 87–96.
[12] S.J. Kernion, K.J. Miller, S. Shen, V. Keylin, J. Huth, M.E. McHenry, IEEE Trans. Magn. 47 (2011) 3452–3455.
[13] M. Kurniawan, V. Keylin, M.E. McHenry, J. Mater. Res. 30 (2015) 2231–2237.
[14] H. Ucar, J.J. Ipus, V. Franco, M.E. McHenry, D.E. Laughlin, JOM 64 (2012) 782–788.
[15] N. Aronhime, V. DeGeorge, V. Keylin, P.R. Ohodnicki, M.E. McHenry, JOM (2017).
[16] V. DeGeorge, E. Zoghlin, V. Keylin, M. McHenry, J. Appl. Phys. 117 (2015), 17A329.
[17] M.E. McHenry, F. Johnson, H. Okumura, T. Ohkubo, V.R.V. Ramanan, D.E. Laughlin, Scr. Mater. 48 (2003) 881–887.
[18] J. Ayers, V. Harris, J. Sprague, W. Elam, H. Jones, Acta Mater. 46 (1998) 1861–1874.
[19] P.R. Ohodnicki, D.E. Laughlin, M.E. Mchenry, M. Widom, Acta Mater. 58 (2010) 4804–4813.
[20] A.M. Leary, M.S. Lucas, P.R. Ohodnicki, S.J. Kernion, L. Mauger, C. Park, C. Kenney-Benson, M.E. McHenry, J. Appl. Phys. 113 (2013) 17–317.
[21] L. Johnson, E. Cornell, D. Bailey, S. Hegyi, IEEE Trans. Power Syst. PAS-101 (1982) 2109–2114.
[22] D. Crespo, T. Pradell, M.T. Clavaguera-Mora, N. Clavaguera, Phys. Rev. B 55 (1997).
[23] E. Pineda, T. Pradell, D. Crespo, N. Clavaguera, M.T. Clavaguera-Mora, J. Non-Cryst. Solids 287 (2001) 92–95.
[24] H. Iwanabe, B. Lu, M.E. McHenry, D.E. Laughlin, J. Appl. Phys. 85 (1999).
[25] M.A. Willard, D.E. Laughlin, M.E. McHenry, D. Thoma, K. Sickafus, J.O. Cross, V.G. Harris, J. Appl. Phys. 84 (1998).
[26] M. Daniil, P.R. Ohodnicki, M.E. McHenry, M.A. Willard, Philos. Mag. 90 (2010) 1547–1565.
[27] I.W. Donald, H.A. Davies, Philos. Mag. A 42 (1980) 277–293.
[28] J. Friedel, in: J.M. Zinman (Ed.) Phys. Met., Cambridge University Press, New York 1969, pp. 340–408.
[29] G.S. Rohrer, Structure and Bonding in Crystalline Materials, Cambridge University Press, Cambridge, 2001.
[30] V.L. Moruzzi, A.R. Williams, J.F. Janak, Phys. Rev. B 15 (1977).
[31] P.R. Ohodnicki, N.C. Cates, D.E. Laughlin, M.E. McHenry, M. Widom, Phys. Rev. B 78 (2008) 144414.
[32] H.E. Kissinger, Anal. Chem. 29 (1957) 1702–1706.
[33] A. Hsiao, M.E. McHenry, D.E. Laughlin, M.J. Kramer, C. Ashe, T. Ohkubo, IEEE Trans. Magn. 38 (2002) 3039–3044.
[34] J.A. Augis, J.E. Bennett, J. Therm. Anal. 13 (1978) 283–292.
[35] S.-G. Zhang, Y. Yu, Mater. Sci. Eng. A 134 (1991) 1008–1011.
[36] M. Abuin, Z. Turgut, N. Aronhime, V. Keylin, A. Leary, V. DeGeorge, J. Horwath, S.L. Semiatin, D.E. Laughlin, M.E. McHenry, Metall. Mater. Trans. A 46 (2015) 5002–5010.
[37] M. De Graef, M.E. McHenry, Structure of Materials: An Introduction to Crystallography, Diffraction and Symmetry, 2nd ed. Cambridge University Press, 2012.
[38] J. Long, P.R. Ohodnicki, D.E. Laughlin, M.E. Mchenry, T. Ohkubo, K. Hono, J. Appl. Phys. 101 (2007).
[39] M.E. McHenry, M.A. Willard, D.E. Laughlin, Prog. Mater. Sci. 44 (1999) 291–433.
[40] C.-W. Chen, Magnetism and Metallurgy of Soft Magnetic Materials, Dover Publications, Amsterdam, 1986.
[41] J.C. Slater, Phys. Rev. 36 (1930) 57–64.
[42] K.A. Gallagher, M.A. Willard, V.N. Zabenkin, D.E. Laughlin, M.E. McHenry, J. Appl. Phys. 85 (1999) 5130.